# Supporting Information

# Rapid synthesis of zeolites through g-$C_3N_4$-based photocatalysis

Yang Liu,[†a, b] Xiao Xue,[†a] Yanshuai Wang,[a, e] Fei Ye,[d] Jian-Guo Dai*[a] and Guohua Chen*[b, c]

[a] Department of Civil and Environmental Engineering, The Hong Kong Polytechnic University, Hung Hom, Hong Kong, China

[b] Department of Mechanical Engineering, The Hong Kong Polytechnic University, Hung Hom, Hong Kong, China

[c] Department of Chemical Engineering, University of Waterloo, 200 University Avenue West, Waterloo, ON, Canada, N2L 3G1

[d] School of Environmental and Chemical Engineering, Yanshan University, Qinhuangdao, China

[e] College of Civil and Transportation Engineering, Shenzhen University, Shenzhen, China

[†]The first two authors contributed equally to this work.

[*]Address correspondence to jian-guo.dai@polyu.edu.hk (J.G. Dai); guohua.chen@polyu.edu.hk (G.H. Chen)

## Materials and Methods

**Raw Materials:** Sodium hydroxide (NaOH, AR, 96%, Sinopharm Chemical Reagent Co., Ltd.); $Na_2SiO_3 \cdot 9H_2O$ (AR, Macklin Chemical Reagent Co., Ltd.); $NaAlO_2$ ($Al_2O_3$ > 41%, Sinopharm Chemical Reagent Co., Ltd.); Melamine (AR, Macklin Chemical Reagent Co., Ltd.); 5,5-Dimethylpyrroline-N-oxide (DMPO, Sigma-Aldrich Co.); Tert-butanol (anhydrous, ≥ 99.5%, Sigma-Aldrich Co.); P-benzoquinone (41%, Sigma-Aldrich Co.)

**Preparation of g-$C_3N_4$**: g-$C_3N_4$ nanosheets were produced from melamine powder according to a modified two-step thermal oxidation method[1,2]. Briefly, 5 g of melamine was put into an alumina crucible with a cover and calcined at 520 °C for 4 h with a heating rate of 5 °C $min^{-1}$. After calcination, the obtained bulk $C_3N_4$ was grounded into powder in an agate mortar. Then, the above powder was put back in an alumina crucible and heated at 580 °C for 1.5 h to prepare the $C_3N_4$ nanosheets. Following that, the resulting powder was dispersed in isopropanol followed by sonication for 8 h. The final products were centrifuged and dried at 60 °C for overnight.

**Photocatalytic synthesis of Na–A ($SiO_2$/0.33$Al_2O_3$/9.51$Na_2O$/77.5$H_2O$) and NaZ-21 ($SiO_2$/0.49$Al_2O_3$/10.2$Na_2O$/77.5$H_2O$)**: In a typical preparation of Na-A (NaZ-21), 24.44 g of $Na_2SiO_3 \cdot 9H_2O$ was dissolved in 60 ml of deionized water with vigorous stirring to obtain solution S1. 4.68 g (6.96 g for NaZ-21) of $NaAlO_2$ and 56.28 g (60 g for NaZ-21) of NaOH were sequentially dissolved in 60 ml of deionized water in a water bath at room temperature to obtain solution S2. Subsequently, solution S2 was added into solution S1 with stirring and the mixture was stirred for 1 hours. The obtained solution was mixed (with or without 50 mg photocatalyst) homogeneously in a Pyrex top-irradiation glass reactor. The synthesis was conducted in dark (aluminum foil covered sample) and under visible light irradiation from the top of the reactor by using a 300 W Xe lamp with a cut-off filter ($\lambda$ > 400 nm) for different time periods (4 h, 6 h, 8 h, 10 h, 12 h, 16 h, 24 h and 58 h). The temperature of the reactant solution was maintained at 25 ± 3 °C by a water bath during the reaction. The obtained

precipitates were separated by centrifugation, washed with deionized water, and then dried at 60 $^{o}$C overnight.

**Theoretical modeling**: Simulation using DFT with generalized gradient approximation (GGA) for exchange-correlation potential embedded in the Vienna Ab Initio Simulation Package (VASP)[3] were calculated and compared with test results from the present experiments and previous literature[4-7]. The ion-electron interaction was described with the projector augmented wave (PAW) method[8]. The cutoff energy of the plane-wave basis set was set at 500 eV. The $[SiO_2(OH)–O–SiO_3]Na_5$ and $[AlO_2(OH)–O–SiO_3]Na_5$ with a periodic boundary condition were modeled with a large super cell of 20 × 20 × 20 Å$^3$, eliminating the artificial interaction between clusters in adjacent cells. The Brillouin zone integrations were performed by using Gamma 1 × 1 × 1 for geometric optimization. The convergence thresholds for structural optimization and transition state (TS) search were set at 0.01 and 0.05 eV/Å in force, respectively. The convergence criterion for energy is $10^{-5}$ eV. The van der Waals (vdW) dispersion by employing the D3 method of Grimme was considered for all the calculation[9]. The climbing image nudged elastic band (CI-NEB) method was used to search the TSs and six images inserted in between two stable states[10].

## Characterization

The microstructure of g-$C_3N_4$ nanosheets and as prepared Na-A zeolite were observed by a scanning electron microscopy (SEM, Hitachi S-4800) and a JEM-2100F scanning transmission electron microscope (STEM) equipped with energy dispersive X-ray (EDX) operated at 200 kV. XPS (KRATOS Analytical, AXIS Ultra DLD) was carried out to analyze the chemical composition of the samples. The UV-vis diffuse spectra (DRS) were measured by a Shimadzu UV-2450 spectrophotometer with the scanning range from 200 to 800 nm. The BET specific surface area was determined by nitrogen adsorption-desorption isotherm measurements at 77 K.

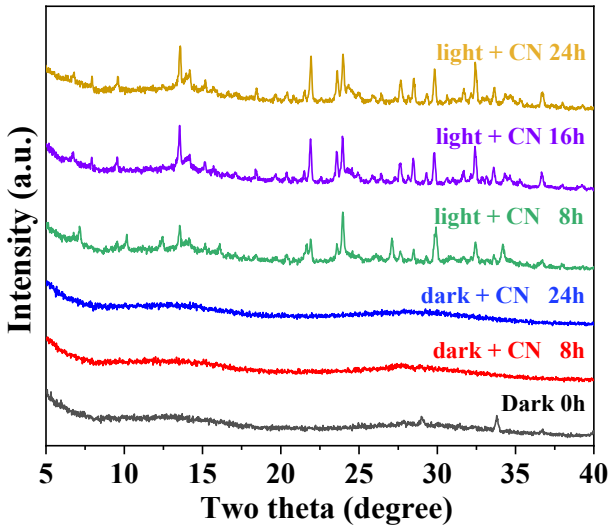


**Fig. S1** XRD of as-prepared NaZ-21 zeolite with different reaction time.

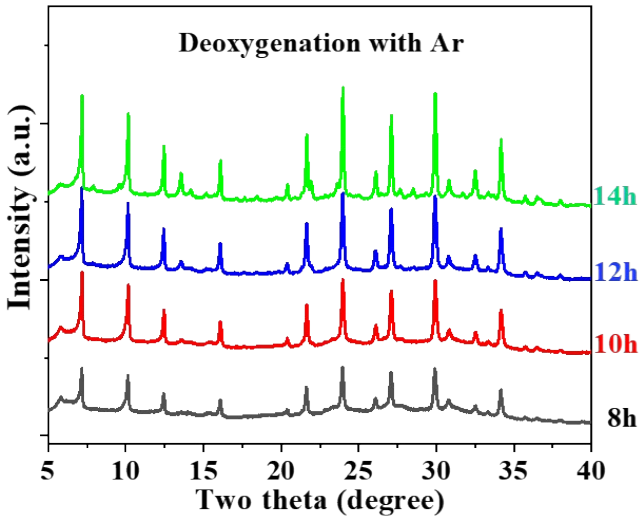


**Fig. S2** XRD of Na-A zeolite with g-$C_3N_4$ and deoxygenated water under visible light irradiation at different reaction time.

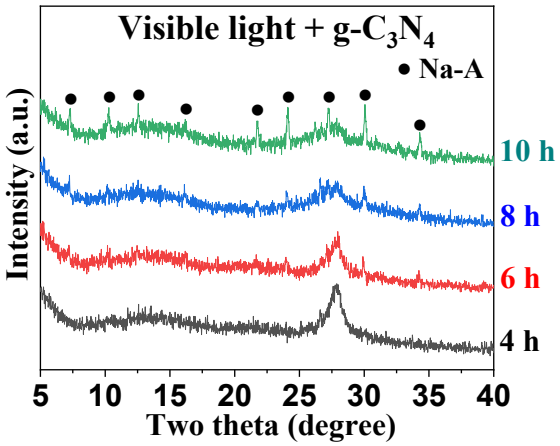


**Fig. S3** XRD of as-prepared Na-A zeolite with different reaction time (repeat).

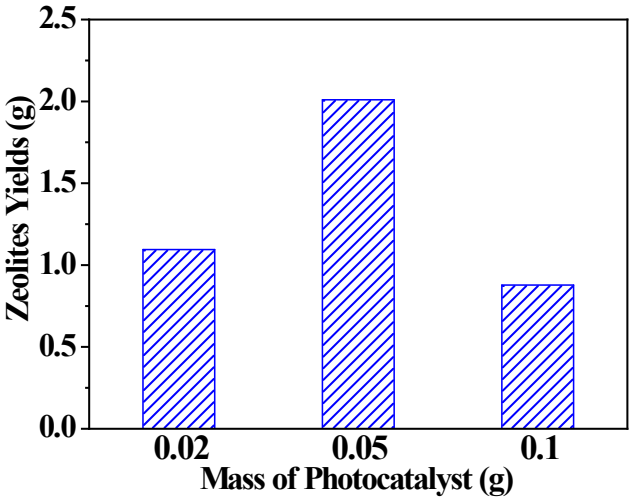


**Fig. S4** Yields of Na-A zeolite with different g-$C_3N_4$ quantities at 8 h.

The XRD patterns of products from photocatalysis with different amount of g-$C_3N_4$ after 8 h irradiation showed that 0.05 g is the optimal amount of photocatalyst for an efficient production of zeolite (Fig. S5). No obvious change was obtained with the increase of photocatalyst, which could be attributed to the less light absorption in the system with high concentration of g-$C_3N_4$. On the other side, less amount of g-$C_3N_4$ lead to the insufficient crystallization of zeolite after 8h indicating that g-$C_3N_4$ is indispensable to the ROS production during photocatalysis process.

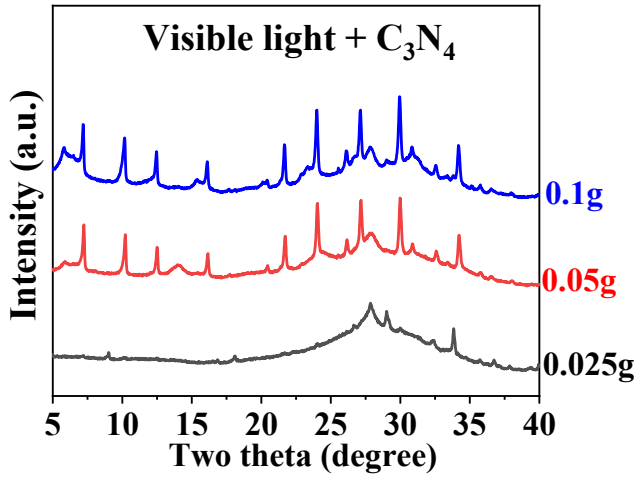


**Fig. S5** XRD patterns of products of zeolite with different amount of g-$C_3N_4$ after 8 h irradiation.

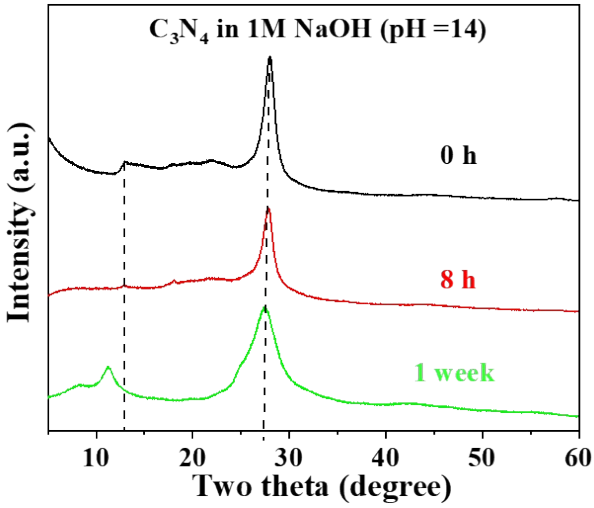


**Fig. S6** XRD of g-$C_3N_4$ in strong basic solution with different time.

**DFT calculation:**

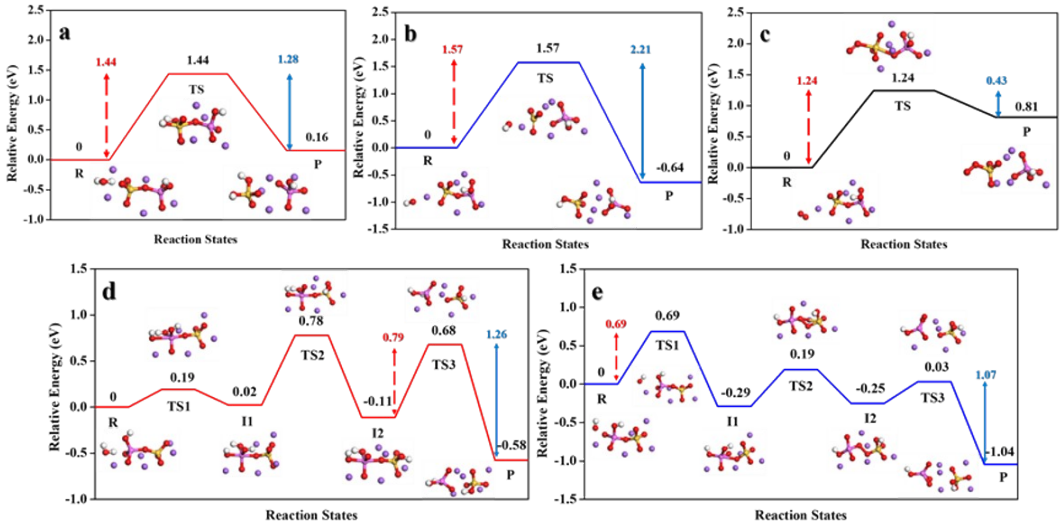


**Fig. S7** Reaction of $[AlO_2(OH)–O–SiO_3]Na_5$ system and Gibbs free-energy calculation. Single-step reaction process (a) $H_2O$, (b) •OH and (c) $•O_2^-$, multi-step reaction processes (d) $H_2O$ and (e) •OH

**SEM analysis:** The morphology of the samples were studied by SEM. The SEM images in Fig. S8a and S8b showed that the product consisted of nanoparticles in the size range 500-1000 nm and some aggregates with grape-like structure. In addition, the nanoparticles were the most general form of the product and the basic unit of the aggregates. Furthermore, the above results indicated that two processes including

crystal growth and structure development occured simultaneously during the 24 h synthesis without photocatalyst under dark.

On the other side, larger nanoparticles aggregates with sheet-like structure were observed in Fig. S8c and S8d. It is worth noting that, the differences of morphology between zeolite and zeolite/g-$C_3N_4$ samples was attributed to the combination of zeolite and g-$C_3N_4$. Furthermore, the sheet-like structure products indicating that g-$C_3N_4$ nanosheets effected the aggregation of zeolite particles during photocatalysis process of zeolite production.

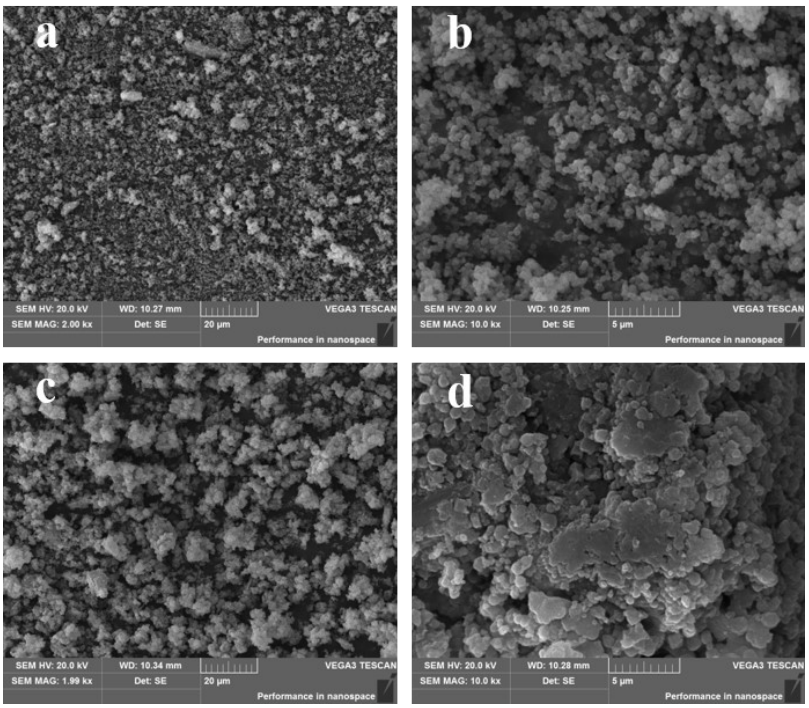


**Fig. S8** SEM of (a, b) Zeolite and (c, d) Zeolite/g-$C_3N_4$.

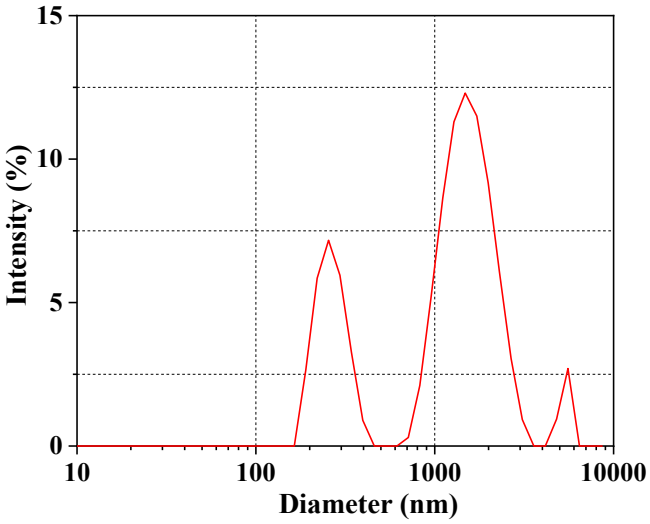


| Solvent | Viscosity (cP) | RI | z-average (nm) | PDI |
|---|---|---|---|---|
| Water | 0.8872 | 1.33 | 933.3 | 0.502 |

**Fig. S9**. Intensity-based DLS data of zeolite/g-$C_3N_4$ in water at 25 °C with Zetasizer software.

**TEM:** As shown in Fig. S10a and S10b, the sample exhibited a few layered sheet-like structure which was attributed to the deposition of zeolite nanoparticles on the g-$C_3N_4$ nanosheets. Further magnification in Fig. S10c showed that the nanoparticles covered on the whole surface of g-$C_3N_4$ nanosheets can be distinguished, indicating the role of g-$C_3N_4$ nanosheets as a substrate during the synthesis process of zeolite. Furthermore, it is reasonable to speculate that a good combination of zeolite and g-$C_3N_4$ nanosheets was achieved.

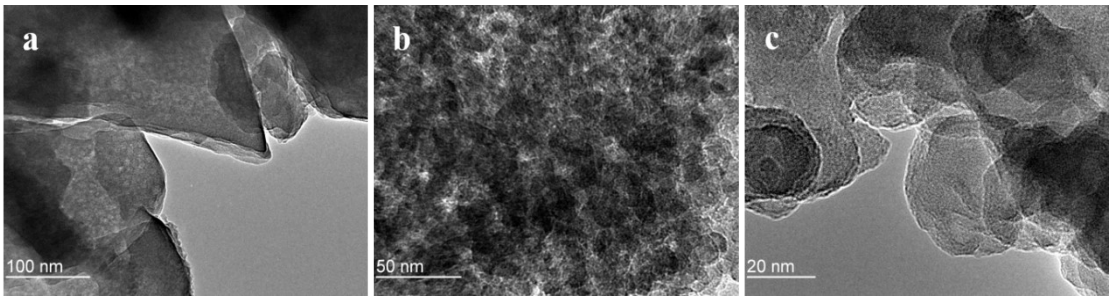


**Fig. S10** TEM of Zeolite/g-$C_3N_4$.

**EDS analysis:** The STEM-EDS (energy-dispersive X-ray spectroscopy) result was shown in Fig. S11. It confirmed that the studied sample consists of Al, Si, O, C and N, which were the main constituent elements of zeolites and g-$C_3N_4$, respectively.

Furthermore, the ratio of component elements has important effect to the as-prepared composite. For zeolite, the framework Si/Al ratio of about 1 in the EDS patten was consistent with Na-A type zeolite. It is worth noted that C and N elements were not in stoichiometric proportion. And this result could be contributed to the broken of g-$C_3N_4$ structure or combination of g-$C_3N_4$ with zeolite. Therefore, further analysis should be carried out to clarify the reason of the phenomenon.

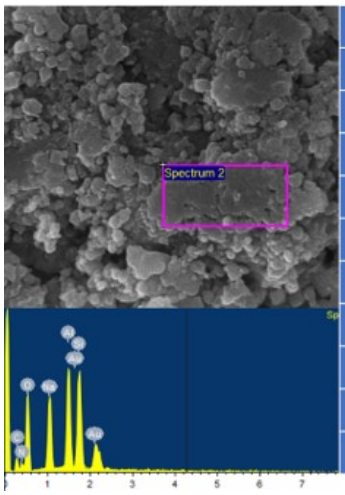


| Element | Weight% | Atomic% |
|---|---|---|
| | | |
| C K | 13.62 | 21.25 |
| N K | 9.76 | 13.06 |
| O K | 36.80 | 43.12 |
| Na K | 9.85 | 8.03 |
| Al K | 9.45 | 6.56 |
| Si K | 10.52 | 7.02 |
| Au M | 10.00 | 0.95 |
| | | |
| Totals | 100.00 | |

**Fig. S11** EDS of Zeolite/g-$C_3N_4$.

**XPS analysis:** The surface composition of a material is commonly characterized by XPS. For zeolite, it is generally considered that, Al, Si, and O are the building elements of zeolite structure and the Si/Al atomic ratio is an indicator of dealumination process on the surface of zeolite structure. The XPS analysis showed that Si/Al atomic ratio of the as-prepared sample was about 1, corresponding to Na-A type zeolite. As shown in Fig. S12a, the peak located at 73.9 eV indicated the presence of aluminosilicate. Fig. S12b showed the XPS spectrum for Si 2*p*. The peak of Si 2*p* was at 101.8 eV corresponding to Si Almand. In Fig. S12c, the O 1s peaks at 531, 531.7 and 536.3 eV was attributed to the C-O bonds, surface hydroxyl groups and Na KLL auger overlap with O1s, respectively. On the other hand, for g-$C_3N_4$, C and N are main constituent elements. The C1s spectra in Fig. S12d. showed three peaks at 284.73, 284.96 and 288.29 eV, which were assigned to $sp^2$ C-C bonds, C-OH bonds and N-C=N bonds in the g-$C_3N_4$ lattice, respectively. The N1s region in Fig. S11e can be fitted into two

peaks at 398.4 eV and 400.2 eV. The peak at 398.4 eV was ascribed to pyridinic nitrogen (C=N–C), which indicated the presence of graphite-like $sp^2$-bonded g-$C_3N_4$. The peak at 400.2 eV corresponded with tertiary nitrogen (N-$(C)_3$). The above results confirmed that the sample was composed of zeolite stucture and g-$C_3N_4$.

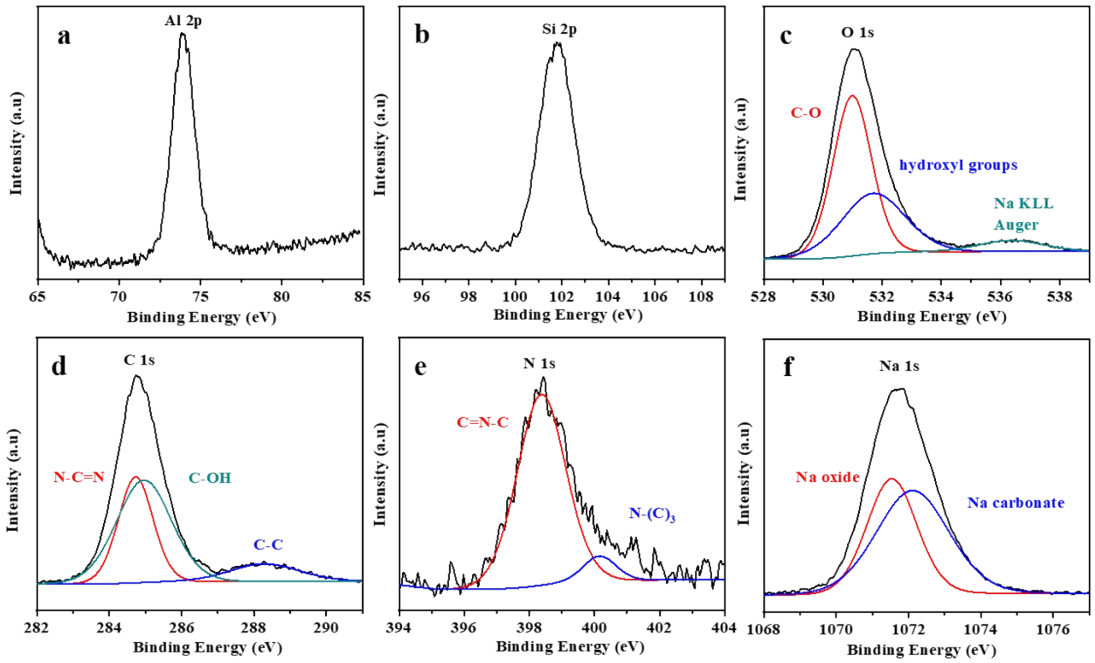


**Fig. S12** XPS of Zeolite/g-$C_3N_4$.

**DRS analysis:** In order to evaluate their light absorption property of the products, the UV-vis diffuse spectroscopy tests of zeolite and zeolite/g-$C_3N_4$ were conducted. As shown in Fig. S13, little light absorption was obtained in the wavelength range between 300 nm and 800 nm because of the white colour of the zeolite. However, compared with zeolite, zeolite/g-$C_3N_4$ exhibited absorption in the UV and visible light regions (from 300 nm to 450 nm), which could be attributed to the existence of g-$C_3N_4$. Furthermore, this light absorption property indicates that the product has a potential for photocatalytic application. Combined with the EDS and XPS results, g-$C_3N_4$ should be stable after reaction and the nonstoichiometric proportion of C and N elements was ascribed to the combination of g-$C_3N_4$ to zeolite.

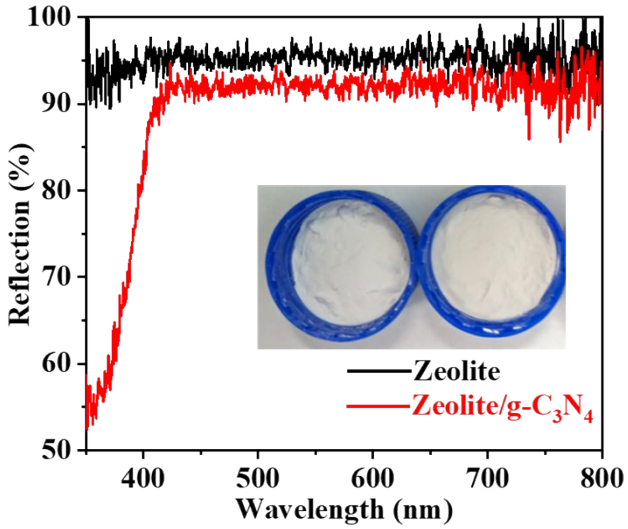


**Fig. S13** Reflection of Zeolite and Zeolite/g-$C_3N_4$.

**BET analysis:** In order to get further information of the structure of product, the Brunauer-Emmett-Teller (BET) specific surface area was investigated by nitrogen adsorption-desorption isotherm measurements. The BET specific surface area of the product was determined to be 50.15 $m^2/g$. In other words, there was still much room for improvement in the porous structure development. Therefore, it is reasonable to extrapolate that the photocatalysis over g-$C_3N_4$ under visible light irradiation has a selective effect on the nucleation and crystal growth processes during the synthesis of Na-A zeolite.

**Application study:** In order to evaluate the photocatalytic activity of product, the methylene blue (MB) degradation was conducted under visible light irradiation. As shown in Fig. S14, after 3 h reaction, the colour of MB solution (20 mg/L) turned from blue to almost clear for the tube with zeolite/g-$C_3N_4$. It is obvious that the g-$C_3N_4$ not only acted as a promoter of zeolite crystallization but also entitles the zeolite with photocatalytic activity, making it have greater potential for applications in environment engineering. This finding is consistent with previous report when zeolite containing g-$C_3N_4$ is used as a photocatalyst for wastewater treatment[11].

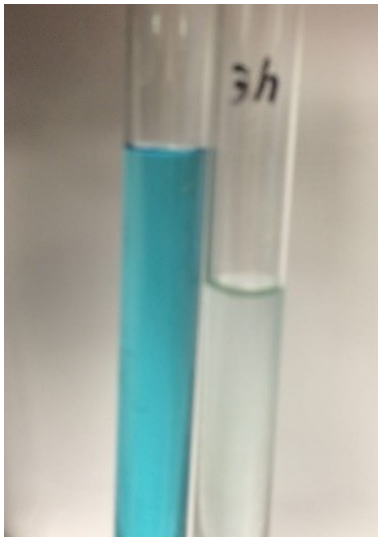


**Fig. S14** Photocatalytic degradation of MB.

Table. S1 Method and parameters for Na-A zeolite synthesis

| Temp. | Time | Method | Aging | Seed | Ref. |
|---|---|---|---|---|---|
| 75-85 °C | 2-3 weeks | hydrothermal | | | 12 |
| 90 °C | 4 h | hydrothermal | | | 13 |
| 100 °C | 12 h | hydrothermal | | | 14 |
| 80 °C | 5 h | hydrothermal | 6 h<br>25 ± 3 °C | 100 °C<br>3-24 h | 15 |
| 90 °C | 5 h | hydrothermal | 5 h<br>30 °C | | 16 |
| 20 °C | 18-45 h | γ-rays | | | 17 |
| 25 ± 3 °C | 8 h | Photocatalysis | | | This work |

**References**


1. S.B. Yang, Y.J. Gong, J.S. Zhang, L. Zhan, L.L. Ma, Z.Y. Fang, R. Vajtai, X.C. Wang and P.M. Ajayan, *Adv. Mater.*, 2013, **25**, 2452-2456.
2. P. Niu, L.L. Zhang, G. Liu and H-M. Cheng, *Adv. Funct. Mater.*, 2012, **22**, 4763-4770.
3. G. Kresse and J. Furthmiiller, *Comp. Mater. Sci.*, 1996, **6**, 15-50.
4. R. Konecny, S. Leonard, X.L. Shi, V. Robinson and V. Castranova, *J. Environ. Pathol. Tox.*, 2001, **20**, 119-132.
5. G.D. Feng, P. Cheng, W.F. Yan, M. Boronat, X. Li, J-H. Su, J.Y. Wang, Y. Li, A. Corma, R.R. Xu and J.H. Yu, *Science*, 2016, **351**, 1188-1191.
6. G. Kresse and J. Hafner, *Phys. Rev. B*, 1993, **47**, 558-561.
7. G. Kresse and D. Joubert, *Phys. Rev. B*, 1999, **59**, 1758-1775.
8. P.E. Blochl, *Phys. Rev. B: Condens. Mater. Phys.*, 1994, **50**, 17953-17979.
9. S. Grimme, J. Antony, S. Ehrlich and H. Krieg, *J. Chem. Phys.*, 2010, **132**, 154104-154119.
10. G. Henkelman, B.P. Uberuaga and H. Jónsson, *J. Chem. Phys.*, 2000, **113**, 9901-9904.
11. J.D. Xiao, Y.B. Xie, J. Rabeah, A. Bruckner and H.B. Cao, *Acc. Chem. Res.*, 2020, **53**, 1024-1033.
12. J. F. Charnell, *J. Cryst. Growth*, 1971, **8**, 291-294.
13. M.K. Seliem and S. Komarneni, *Micropor. and Mesopor. Mat.*, 2016, **228**, 266-274.
14. J.L.X. Hong, T. Maneerung, S.N. Koh, S. Kawi and C-H. Wang, *Ind. Eng. Chem. Res.*, 2017, **56**, 11565-11574.
15. H.Z. Li, C.L. Qiu, S.J. Ren, Q.B. Dong, S.X. Zhang, F.L. Zhou, X.H. Liang, J.G. Wang, S.G. Li and M. Yu, *Science*, 2020, **367**, 667-671.
16. W-R. Lim, C-H. Lee and S-Y. Hamm, *Mater. Chem. Phys.*, 2021, **261**, 124230.
17. X.Q. Chen, M.H. Qiu, S.G. Li, C.G. Yang, L. Shi, Shiju Zhou, Gan Yu, Lixia Ge,

Xing Yu, Ziyu Liu, Nannan Sun, Kun Zhang, Hui Wang, Mouhua Wang, Liangshu Zhong and Yuhan Sun, *Angew. Chem., Int. Ed.*, 2020, **59**, 11325-11329.